Sensors and Materials, Vol. 38, No. 1 (2026) 71–88
MYU Tokyo

S & M 4284

Traction Microsystem with Force Sensing for Colon Endoscopic Submucosal Dissection

Xinchi Gao,[1] Noriko Tsuruoka,[2*] Wenrui Liu,[1] Yuto Sakaguchi,[2]
Yosuke Tsuji,[3] Mitsuhiro Fujishiro,[3] Fumihito Arai,[4] and Yoichi Haga[1,2]

[1]Graduate School of Biomedical Engineering, Tohoku University,
Aza-Aoba, Aramaki, Aoba-ku, Sendai 980-8579, Japan
[2]Graduate School of Engineering, Tohoku University, Aza-Aoba, Aramaki, Aoba-ku, Sendai 980-8579, Japan
[3]Graduate School of Medicine, The University of Tokyo, 7-3-1 Hongo, Bunkyo-ku, Tokyo 113-8655, Japan
[4]Graduate School of Engineering, The University of Tokyo, 7-3-1 Hongo, Bunkyo-ku, Tokyo 113-8656, Japan

(Received November 14, 2025; accepted December 23, 2025)

Keywords: ESD, traction, force sensor, slip ring, strain gauge, flexible endoscope

Endoscopic submucosal dissection enables the en bloc resection of colorectal lesions with curative intent for early cancers, but it is technically demanding and carries risks such as bleeding and perforation, partly due to limited visualization within the submucosal layer. A narrow field of view, curled incision edges, and insufficient traction can obscure the cutting plane and increase procedural difficulty. Effective traction is critical for improving visibility and facilitating safer resections, yet common methods such as clip-with-line often add procedural complexity and lack real-time force monitoring. We present a traction microsystem that integrates a micromotor, a slip ring, and a miniaturized force-sensing unit into an endoscope-deliverable module. The slip ring allows continuous rotation without torsional buildup, maintaining stable tension during operation. The force sensor utilizes a 3D-printed flexure with a strain gauge to amplify deformation, achieving high sensitivity in a compact form that enables real-time force readouts. This architecture supports controlled mucosal lifting with feedback-guided traction, enhancing submucosal exposure and potentially improving resection accuracy and safety.

1. Introduction

Endoscopic submucosal dissection (ESD) represents a significant advancement in the minimally invasive treatment of early-stage gastrointestinal neoplasms. By enabling the en bloc resection of large lesions, ESD offers superior pathological staging and lower local recurrence rates than conventional endoscopic mucosal resection.(1) Despite these advantages, ESD remains a technically demanding procedure, particularly within the colon. The colon's thin wall, tortuous anatomy, and constant peristalsis increase the complexity and risk of the operation, leading to longer procedure times and a higher incidence of complications such as bleeding and perforation.(2) Central to overcoming these challenges is the application of effective and

---

[*] Corresponding author: e-mail: noriko.tsuruoka@tohoku.ac.jp
https://doi.org/10.18494/SAM6028

ISSN 0914-4935 © MYU K.K.
https://myukk.org/

consistent traction. Adequate traction is crucial for lifting the mucosal flap away from the underlying muscularis propria, thereby creating a clear and stable view of the submucosal layer. This enhanced visualization allows the endoscopist to accurately identify the dissection plane and crucial blood vessels, which is essential for ensuring a safe and efficient resection.(3) However, a major limitation across current traction methodologies is the inability to objectively monitor and control the applied force. Insufficient tension results in poor visualization, whereas excessive force can cause tissue tearing or perforation, undermining the safety of the procedure. This gap underscores a critical need for an intelligent traction system that can provide real-time, quantitative feedback to the operator.

Multiple traction strategies have been proposed and evaluated for ESD (Fig. 1), each with inherent strengths and limitations. The clip-with-line method, for instance, is valued for its simplicity and low cost, but is often limited by a unidirectional pulling force that may not be optimal for all lesion locations.(4,5) Internal traction devices, such as the S-O clip (Sakamoto-Osada clip) and multi-loop systems, offer the advantage of being independent of endoscope movement but typically provide a passive, uncontrolled tension.(6) More complex approaches, like the double-scope technique, allow for dynamic, multi-directional traction but at the cost of requiring two endoscopists and specialized setups, which limits their widespread applicability.(7) The pocket-creation method is a strategic approach that improves traction by creating a submucosal tunnel, but its effectiveness can be limited in cases with severe fibrosis.(3) While these methods have incrementally improved the feasibility of ESD, none have successfully addressed the dual challenges of providing an intraluminal anchor and enabling real-time, active control over traction forces. To address the challenges in colorectal ESD, particularly the need for effective and stable traction, we present an integrated traction system that provides controllable traction and real-time force feedback while remaining compatible with the conventional ESD workflow. The purpose of this research is to develop a compact module that can be delivered through a standard endoscope, improve submucosal visualization, reduce the risk of complications related to traction, and prepare the system for future traction control based on feedback. In this section, we describe in detail the design principles, overall architecture, and fabrication processes of the key components of this system.

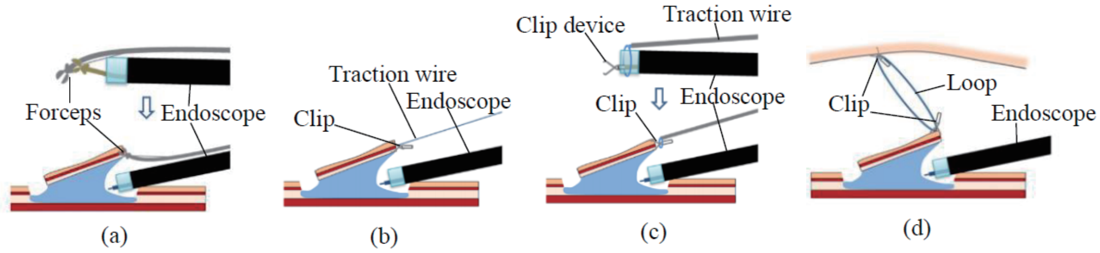

Fig. 1. (Color online) Representative traction methods for colorectal ESD: (a) external forceps method, (b) clip-with-line method, (c) clip-and-snare method with a prelooping technique, and (d) clip-with-loops method.(2)

2. System Design and Fabrication

The primary objective is to develop a device that can be endoscope-deliverable, provide stable anchorage within the complex colonic environment, and apply precisely controlled traction force to the lesion, thereby improving surgical visualization and safety. The system comprises two core elements: (1) an expandable spiral scaffold that provides a stable working platform(8) (Fig. 2) and (2) a traction microsystem that applies mechanical traction and incorporates an integrated force sensor for real-time feedback.

2.1 System architecture

The proposed system consists of an expandable spiral scaffold and a traction microsystem. Here, the traction microsystem denotes a miniaturized traction Cybernetic Avatar (CA) combined with an integrated force sensor, positioned as an in-body CA module within the Moonshot project.(9) The scaffold provides a stable platform in the colonic lumen, while the traction microsystem generates controlled traction and measures the resulting force in real time. The traction microsystem is conceived as a modular platform compatible with standard endoscopic workflows. The architecture can be conceptually divided into an in-body subsystem operating within the colon and an external subsystem for external control and data acquisition.

The delivery and deployment of the in-body subsystem is the initial procedural step. The scaffold preloaded with the traction microsystem is introduced transanally through a conventional colonoscopy overtube (ST-CB1, Olympus). The overtube is navigated to the target lesion with a flexible endoscope as shown in Fig. 3(a) and is then left in place to serve as a delivery conduit as shown in Fig. 3(b). To pass through an overtube with an inner diameter of approximately 10 mm, the entire in-body assembly, including the traction microsystem rolled within the scaffold, must collapse to a diameter smaller than this constraint. After the overtube is positioned, the rolled scaffold assembly is advanced through its lumen under endoscopic guidance as shown in Fig. 3(c). When the assembly reaches the target site, the scaffold is extruded from the overtube and expanded pneumatically using pressurized gas supplied through a thin silicone tube. The scaffold transforms into its functional spiral geometry and forms a

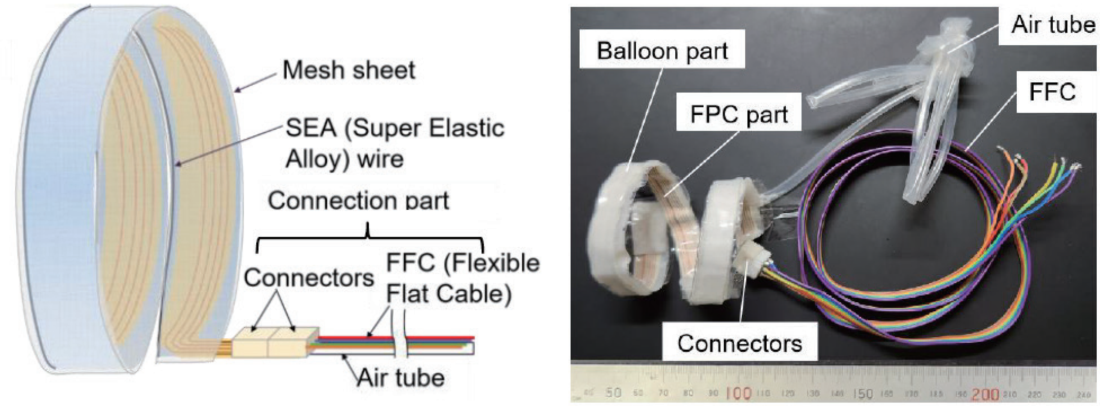

Fig. 2. (Color online) Oblique view of the scaffold (left) and fabricated scaffold (right).(8)

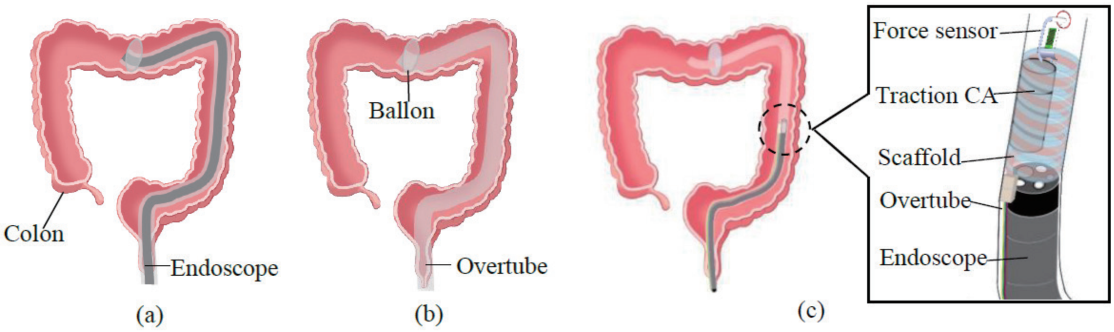

Fig. 3. (Color online) Delivery process of scaffold and CA: (a) insertion of overtube, (b) left overtube in colon,(8) and (c) delivery of scaffold and traction microsystem.

stable intraluminal anchoring platform while avoiding excessive radial pressure on the colonic wall, as shown in Fig. 4(a).

The in-body subsystem is the core of the traction platform. The outer casing of the traction CA is bonded to the scaffold's exterior with silicone resin adhesive. Electrical power and control signals are delivered from the external unit to the CA through a flexible printed circuit embedded in the scaffold. The foundational component is an air-driven spiral scaffold (Fig. 2) fabricated from a soft silicone sheet. When inflated, it anchors gently against the colonic wall, and its spiral geometry maintains lumen patency. To enhance stability and deployment, the scaffold includes an outer mesh layer that increases friction and an embedded, preshaped super elastic alloy (SEA) wire that ensures reliable expansion.(8) The traction microsystem mechanism comprises the traction CA and an integrated force sensor [Fig. 4(a)]. These are linked by a lead wire that transmits both mechanical traction and the electrical signal from the force sensor. A small ring is fixed to an aperture at the distal end of the force sensor to facilitate grasping and fixation by a clip device.

The procedure begins once the scaffold is securely anchored [Fig. 4(a)]. Under endoscopic guidance, a clip device is advanced through the endoscope's instrument channel [Fig. 4(b)]. The clip is passed through the ring at the distal end of the force sensor and then used to grasp the proximal edge of the lesion [Fig. 4(c)]. After the clip is released [Fig. 4(d)], the traction microsystem is actuated via the external control unit. By precisely winding the lead wire, the CA applies a controlled and stable traction force to the lesion. This elevates the mucosal flap and exposes the submucosal layer, providing a clear field for dissection with a rotatable and articulating (RA) knife [Fig. 4(e)].

The external subsystem includes a microcontroller and motor driver to operate the CA and a data acquisition module that processes and displays real-time force data from the sensor, providing continuous feedback to the operator throughout the procedure. After resection, the CA can be used to retrieve the specimen, and the assembly is then deflated and removed through the overtube [Fig. 4(f)].

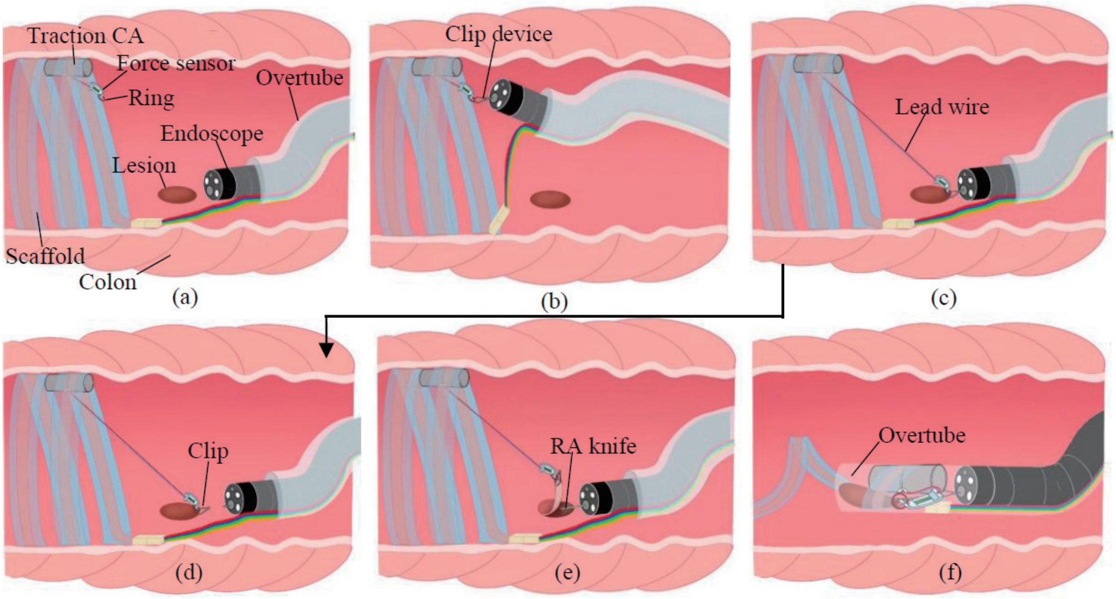

Fig. 4. (Color online) Traction process. (a) Inflate the scaffold. (b) Grasp the ring with clip under endoscopic guidance. (c) Attach the clip to the proximal end of the lesion. (d) Release the clip. (e) Cut the lesion. (f) Retrieve the resected lesion and scaffold with traction microsystem.

2.2 Design and fabrication of traction CA

The design of the traction CA main body was driven by two requirements: a compact form factor compatible with endoscopic delivery and sufficient output to generate effective lesion traction. Actuator selection was guided by typical forces applied during clinical ESD. Operators often use the weight of a 5 g gauze (≈ 0.05 N) as a practical traction level. To meet this requirement while keeping the actuator as compact as possible, a 6-mm-diameter DC gear motor (NFP-609-136-0675, Need for Power Electronics) was selected. The motor can deliver up to about 2.1 N, providing a comfortable margin over the clinically required force and supporting reliable traction. The overall structure of the traction system and the integration of the force sensor are illustrated in Fig. 5.

The motor drives a custom dual-hole reel with a 3 mm central shaft and 6 mm outer flanges, designed to accommodate the 0.4 mm lead wire. The calculated wire take-up capacity is 277.2 mm, which exceeds the theoretical maximum traction distance of 64 mm. Because the force sensor is integrated at the distal end of this lead wire, the sensor signal must be routed through the rotating reel. An integrated slip ring (LPMS-04A, JNPAT Electronics) provides continuous electrical connection, preventing wire twisting during winding and ensuring stable signal transmission.

To protect the electromechanical components from the complex and humid intracolonic environment, a fully enclosed waterproof casing was designed. Thickness testing indicated that a wall thickness of 0.6 mm provides an optional effective balance between mechanical robustness and compact size, maintaining casing integrity during delivery. The casing was

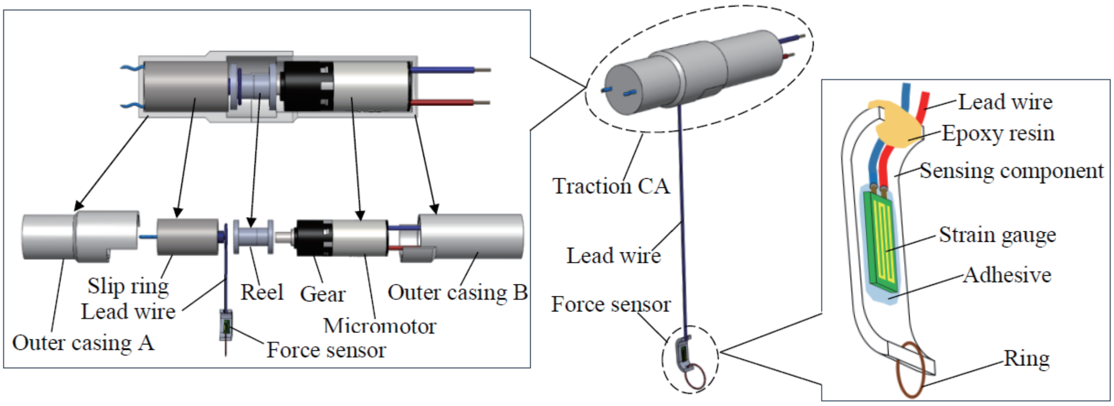

Fig. 5. (Color online) Structure of traction microsystem.

fabricated with a high-precision 3D printer (Agilista, Keyence), enabling a compact interior that accurately houses the motor and the slip ring. The assembled traction CA module measures 37.6 mm in length and 8.6 mm in diameter [Fig. 6(b)]. These dimensions were chosen to ensure safe delivery through a standard colonoscopy overtube. A fabricated prototype of the complete device is shown in Fig. 7.

The control system of the traction microsystem comprises a control board (Arduino Uno, Arduino), a motor driver (TB6612FNG, Toshiba), and a joystick for operator input. The Arduino Uno samples the joystick's analog signal and generates corresponding pulse-width modulation commands (Fig. 8). These commands are sent to the motor driver that regulates power to the DC motor and enables precise bidirectional rotation. The operator winds the lead wire to apply traction and unwinds it to release tension.

We evaluated the traction capability of the traction CA. The micromotor has a stall torque of 100 g·cm and a rated speed of 175 ± 15% rpm. At present, there is no standardized numerical guideline specifying the appropriate traction force for ESD. Existing clinical studies describe traction only in qualitative terms, such as gentle, adequate, or excessive,(10) because the optimal traction depends strongly on the mechanical properties of each lesion. Factors such as fibrosis, lesion thickness, submucosal stiffness, and local wall strength vary considerably among patients and across different regions of the colon. This large variability makes it difficult to define a quantitative range that applies to all clinical situations. Given the absence of an established clinical standard, we defined a working range of traction forces for this study by combining current clinical practice with the results of the *ex vivo* safety evaluations.

In routine ESD procedures, a 5 g gauze is used as a reference traction weight, which corresponds to approximately 0.05 N. Endoscopists regard this force level as reliably producing a useful mucosal lifting effect. To determine an appropriate upper limit of traction force, we conducted two bench tests. In the ring detachment test using a standard endoscopic clip (Fig. 9), the ring was secured to the closed clip and the traction wire was connected to a force gauge. Tensile load was gradually increased by pulling the wire through the force gauge until detachment occurred. This test was repeated ten times, and the detachment force ranged from 1.07 to 1.37 N, with an average of 1.29 N.

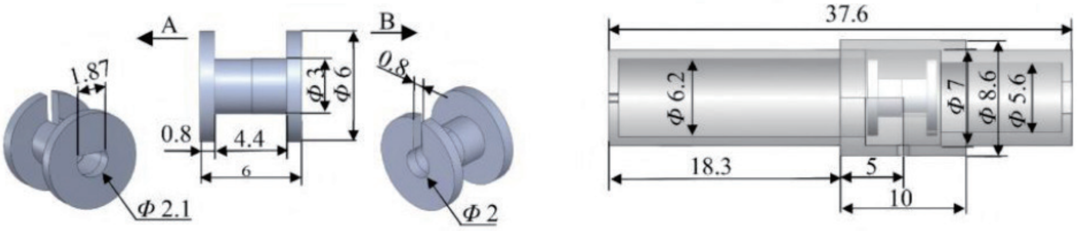

(a) (b)

Fig. 6. (Color online) Dimensions of (a) reel and (b) reel inside the outer casing (all dimensions are in mm).

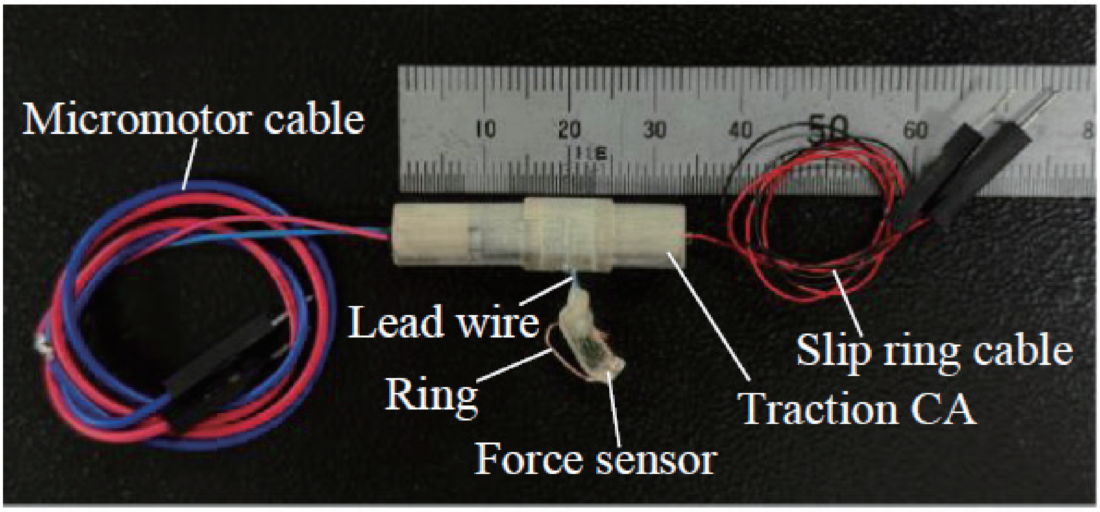

Fig. 7. (Color online) Fabricated prototype of traction microsystem.

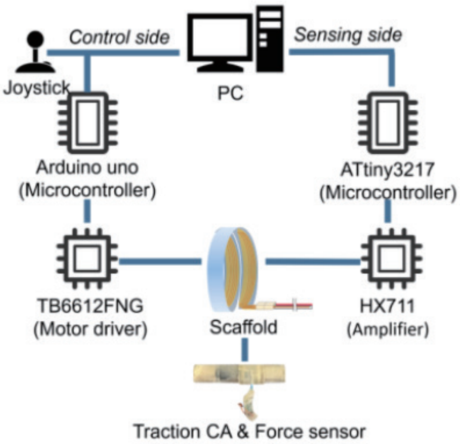

Fig. 8. (Color online) Schematic of control and data acquisition system architecture.

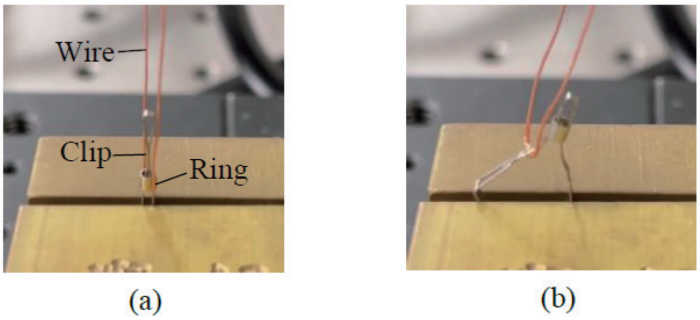

(a) (b)

Fig. 9. (Color online) Clip–ring detachment force measurement. (a) Ring secure the closed clip. (b) Pull the ring until detachment occurs.

In the safety tension test performed on the excised porcine colon (Fig. 10), a standard endoscopic clip was attached to the mucosa and the traction wire was connected to a force gauge. Tensile force was gradually increased by pulling the wire through the force gauge until either clip detachment or tissue tearing occurred. This test was repeated ten times, and clip detachment or tissue tearing occurred at forces between 0.66 and 1.39 N, with an average of 1.01 N. To maintain a conservative safety margin relative to potential tissue failure, we adopted 0.66 N, the lowest observed failure load, as the upper bound of the intended operating range. As a result, the working traction force range in this study was defined as 0.05 to 0.66 N. Note that the porcine tissue used in this test represents healthy mucosa. In actual ESD, many lesions are fibrotic or thickened, and their mechanical strength is generally higher than that of normal tissue. Therefore, the failure forces obtained here should be regarded as conservative estimates of clinical tolerance.

The proposed system provides a peak traction capability of approximately 2.1 N. This level is well above the required working range and provides a sufficient safety margin. When used within the defined operating window of 0.05 to 0.66 N, the traction microsystem can apply stable and controllable lifting forces. This allows the operator to make fine adjustments during ESD while satisfying clinically relevant traction requirements and accommodating variations in the mechanical properties of different lesions. We also assessed the retraction and extension of the lead wire. The traction CA smoothly extended and retracted up to 120 mm of the lead wire without obstruction, jamming, or adverse effects on traction, confirming the reliability and practicality of the mechanical structure.

2.3 Design and fabrication of force sensor

The force sensor was developed to address two drawbacks of a previous design.(11) First, its structural configuration was sensitive to load direction, which precluded the accurate measurement of the total traction force [Fig. 11(a)]. Second, the bulky cross-section of the previous CA body impeded efficient delivery because the force sensor was located inside the CA body, and it restricted further miniaturization and integration with other components. The goal of the present iteration was to create a compact, highly sensitive sensor positioned between the

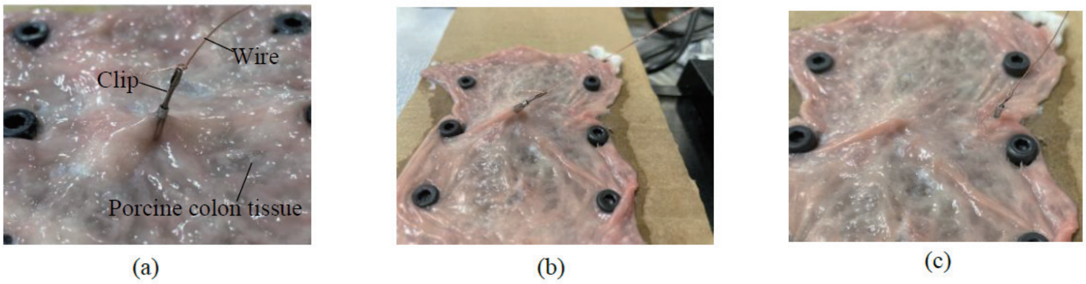

Fig. 10. (Color online) Safety tension force test. (a) Tie the wire on the clip. (b) Apply constant tension. (c) Observe clip detachment.

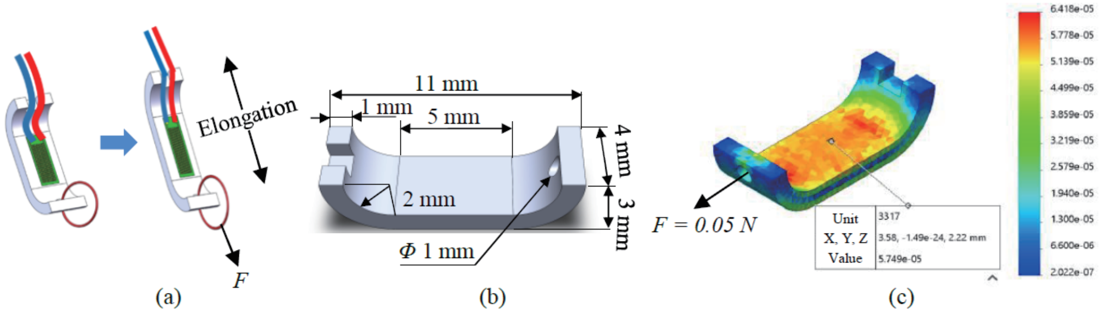

Fig. 11. (Color online) Analysis and dimensions of the force sensor's sensing component. (a) Sensing mechanism of the force sensor. (b) Key dimensions of the sensing component. (c) Strain distribution on the sensing part under a 0.05 N load (finite element analysis in SOLIDWORKS®).

CA lead wire and the endoscopic clip so that it measures the uniaxial traction force applied directly to the lesion. The force sensor is placed in series with the lead wire and measures the axial tension transmitted through the wire, rather than the contact force directly at the lesion. The sensor operates by converting traction-induced mechanical strain into an electrical signal.

In an idealized configuration with a straight lead wire path and negligible friction, the lead wire tension equals the traction force transmitted to the lesion. In actual ESD procedures, however, the force acting on the lesion can differ from the measured tension because of friction at the traction ring, the bending of the wire along the endoscopic channel, and the angle between the wire and the local lesion surface. Therefore, in this study, we interpret the measured wire tension as a quantitative index of the traction level rather than as an exact value of the force at the lesion.

The core element is a 3D-printed sensing board with a curved recessed geometry optimized to amplify deformation [Fig. 11(b)]. Finite element analysis confirmed that, under the same applied load, this geometry produces a greater strain than a flat beam, thereby improving sensitivity [Fig. 11(c)]. The sensing element is a 9.5 × 4 mm^2 foil strain gauge (GFLAB-3-50, Tokyo Measuring Instruments Laboratory).

The fabrication and assembly were planned to ensure both accuracy and robustness. The sensing board, which integrates a front ring, was first fabricated with overall dimensions of 11 mm in length, 3 mm in height, and 4 mm in width [Fig. 11(b)]. A 0.4 mm lead wire composed of 11 twisted strands of copper–silver alloy with polyurethane insulation (polyurethane-coated copper–silver litz wire) was selected for its strength, flexibility, and conductivity. Its breaking load of 36 N provides a large safety margin relative to clinical traction forces.

During assembly, the lead wires were soldered to the strain gauge [Fig. 12(a)]. The prewired strain gauge was then bonded to the flat central surface inside the recessed region of the sensing board [Fig. 12(b)]. To protect the solder joints from mechanical stress during traction, the lead wires were secured at the board end with epoxy resin (Araldite, Nichiban Co., Ltd.), which acts as strain relief and prevents pull forces from being transmitted to the solder points. After assembly, a protective layer was applied over the strain gauge and recessed area (SB tape, Tokyo Measuring Instruments Laboratory) to shield the sensing element from the external environment.

The data acquisition system for the force sensor consists of three components (Fig. 8): the strain gauge forming one arm of a Wheatstone bridge with three precision resistors, a signal amplifier with a programmable-gain stage (HX711, Avia Semiconductor), and a microcontroller (ATtiny3217, Microchip Technology). In operation, traction-induced strain changes the gauge resistance, producing a small bridge imbalance that the HX711 amplifies and digitizes to a high-resolution value. The ATtiny3217 then reads and processes this value to compute the real-time traction force.

3. Experimental Methods

3.1 Experimental setup

In this section, we discuss a comprehensive experimental evaluation of the sensor's performance, focusing on static characteristics, repeatability, and dynamic tracking. The sensor uses a strain gauge that converts mechanical strain (ϵ) into a change in electrical resistance (ΔR). The proportionality is set by the gauge factor (GF), a parameter specified by the manufacturer. Let R be the nominal resistance of the gauge. The relationship is

$$\epsilon = (\Delta R / R_0) / GF \tag{1}$$

where R_0 is the initial nominal resistance of the gauge.

In this system, the measurand is force (F). We therefore require a model that links the measurable strain ϵ to the applied force. Within the sensor's designed operating range, which lies in the linear elastic region, we assume a linear relation characterized by the sensitivity coefficient (S), as shown in Eq. (2).

$$\epsilon = S \cdot F \tag{2}$$

Combining Eqs. (1) and (2) allows force to be inferred from the measured resistance change (ΔR). In the following sections, we focus on experimentally determining S in units of ϵ/N through calibration. This calibration provides the quantitative basis for all subsequent performance analyses.

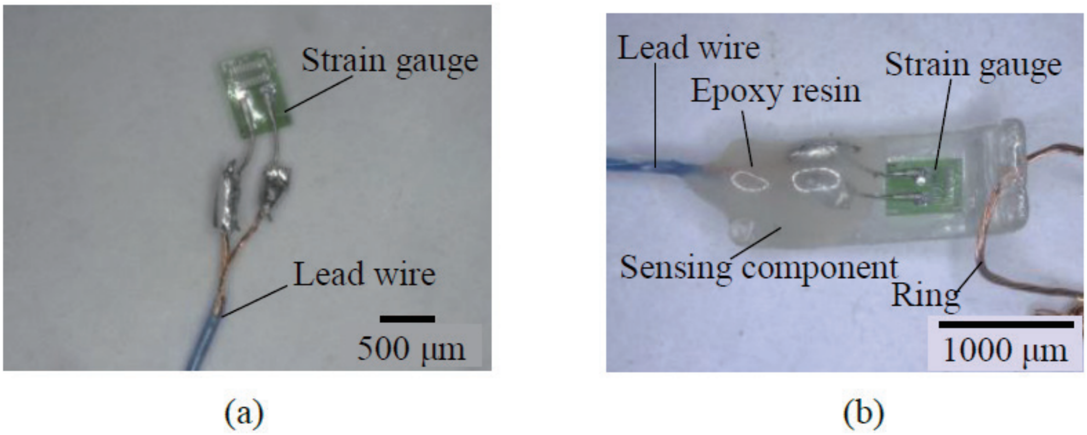

Fig. 12. (Color online) Fabrication of the force sensor component. (a) Strain gauge after being soldered to lead wires. (b) Final sensor prototype with the strain gauge mounted onto the sensing component.

To test the system's performance, a complete experimental platform was constructed, as depicted in Fig. 13. This platform integrates the mechanical fixtures, the control system, and the data acquisition system described in previous sections, which is designed to apply and measure controlled tensile loads. In this configuration, the lead wire was aligned with the loading direction and no additional pulleys or bends were introduced, so the tension measured by the sensor closely approximated the applied tensile force. The operational workflow is as follows: the operator uses the joystick module to send control commands to the Arduino Uno microcontroller. The microcontroller, in turn, drives the micromotor, which controls the retraction and extension of the lead wire. This lead wire applies a precise pulling force to the force sensor. The sensor detects this applied force, and its signal is processed by the sensing circuitry. Finally, all digitized force data are transmitted in real time from the microcontroller to a host PC via a USB serial port. Custom data acquisition software running on the PC is responsible for the synchronous recording, display, and storage of the experimental data.

3.2 Static characterization

The static characterization assessed fundamental metrological performance under quasi-static loading, focusing on linearity and hysteresis. As shown in Fig. 14, a step-loading protocol was used. Four identical 5.76 g weights were added to the sensor sequentially, one at a time, until the maximum load was reached; the weights were then removed in reverse order. After each load change, the load was held for approximately 10 s to record the steady-state output.

3.3 Repeatability assessment

To evaluate the sensor's repeatability, defined as its ability to produce consistent outputs under identical conditions, a dedicated loading test was conducted (Fig. 15). Each test cycle

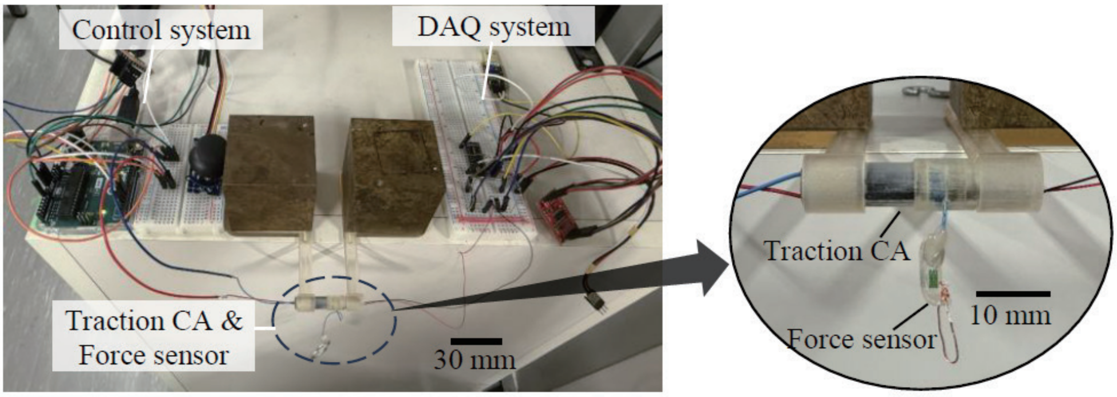

Fig. 13. (Color online) Experimental platform for force sensor system performance evaluation.

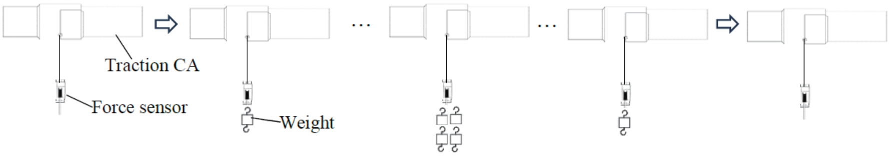

Fig. 14. Schematic of the step-loading procedure for static characterization.

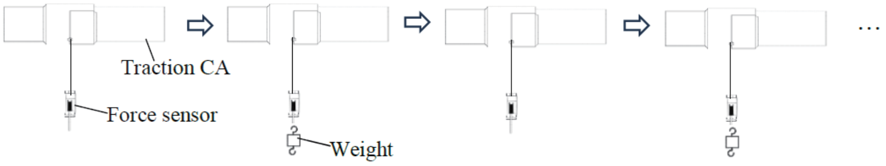

Fig. 15. Schematic of experimental procedure for repeatability assessment.

included three steps: apply a fixed weight, hold for 10 s to record the stable output, then remove the weight and hold for 10 s to record the zero-point reading. This loading and unloading cycle was performed three times in a row. Repeatability was quantified from the three stable readings at the applied load and the corresponding zero-point returns. Two complementary metrics were reported as a percentage of full-scale output (FSO).

3.4 Dynamic performance validation

The objective of this experiment was to assess the sensor's consistency and dynamic response under time-varying tensile forces. The sensor prototype was connected in series with a high-precision commercial force gauge (ZTS-20N, IMADA) that served as the reference (Fig. 16). During testing, the traction CA tightened the lead wire to generate traction. The force sensor and the reference gauge were connected in series, so the same interaction force was transmitted through both devices and recorded simultaneously. Outputs from the sensor and reference gauge were acquired at the same time for direct comparison.

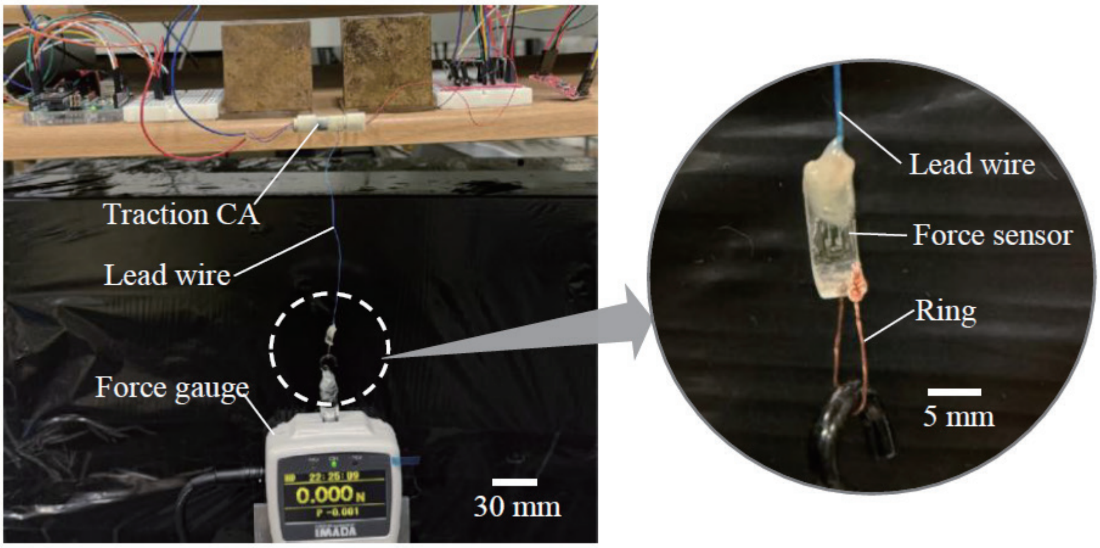

Fig. 16. (Color online) Experimental platform for force sensor system dynamic performance validation.

4. Evaluation Results

4.1 Static performance

The qualitative result is shown in Fig. 17(a). In the figure, the orange trace is the applied reference force and the green trace is the force measured by the sensor. The sensor output closely follows the step changes during both loading and unloading, and the plateaus at each level are stable, indicating good response under constant loads.

Figure 17(b) provides a direct comparison of the sensor outputs during loading and unloading. The loading curve in orange and the unloading curve in green nearly overlap across the full range, indicating low hysteresis and excellent consistency within the tested forces of approximately 0 to 0.23 N.

For quantitative analysis, the first three seconds after each step change and the last three seconds before the next step change were excluded so that only the steady-state response was evaluated. Linearity and accuracy metrics are summarized in Table 1. The coefficient of determination was R^2 = 0.992 and the Pearson correlation coefficient was r = 0.996, demonstrating a very strong linear relationship between the applied force and the sensor readings. The mean absolute error was MAE = 0.005018 N and the root mean square error was $RMSE$ = 0.005451 N, indicating high static accuracy and precision.

In conclusion, the static evaluation demonstrates that the force sensor exhibits high linearity, accuracy, and low hysteresis, supporting its reliability for precise force measurement in this application.

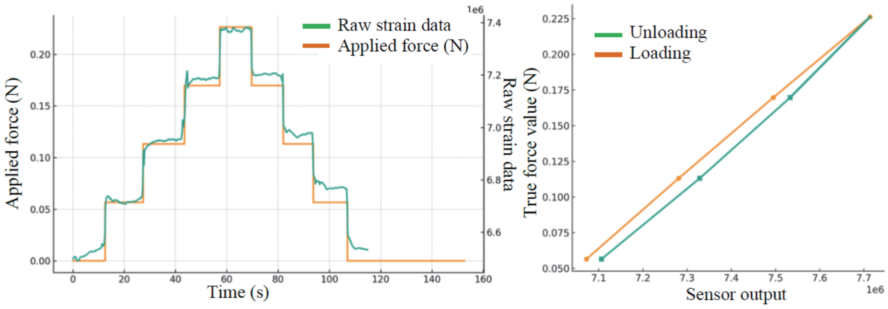

(a) (b)

Fig. 17. (Color online) Static characterization of force sensor. (a) Response to step input forces. (b) Correlation between applied load and sensor output.

Table 1
Statistical evaluation results from static characterization.

R^2	*Corr* (r)	*MAE* (N)	*RMSE* (N)
0.992	0.996	0.005018	0.005451

4.2 Repeatability

To evaluate repeatability, raw strain data from three independent step loading–unloading tests under the same nominal force sequence are shown in Fig. 18. As illustrated, distinct step responses and stable plateaus appear at each load level in all three tests, confirming that the sensor can clearly resolve changes in applied force. Small offsets between tests and slight drifts during the holding periods are also evident, indicating repeatability errors and time-dependent effects that are quantified below. For each test, the mean steady-state output was computed. The basic values used for calculation are listed in Table 2. The repeatability error, expressed as standard deviation and reported as a percentage of full-scale output, ranged from about 0.56% to 1.12% FSO, with an overall average of about 0.84% FSO. For reference, commercial foil strain-gauge sensors are often specified at less than 0.2% FSO under controlled laboratory conditions, so the prototype shows higher variation.

The observed deviation likely arises from several factors. In addition to minor inconsistencies from manual loading and insufficient stabilization time, contributing causes may include viscoelastic effects of the 3D-printed substrate, adhesive creep around the gauge, and thermal drift.

4.3 Dynamic tracking performance

During the dynamic validation test, the outputs of the prototype sensor and reference force gauge were recorded simultaneously with a sampling period of 0.1 s (10 Hz). The qualitative result is shown in Fig. 19. The prototype trace in blue closely follows the reference gauge trace in orange throughout loading and unloading, with minimal observable lag, indicating high responsiveness and sensitivity.

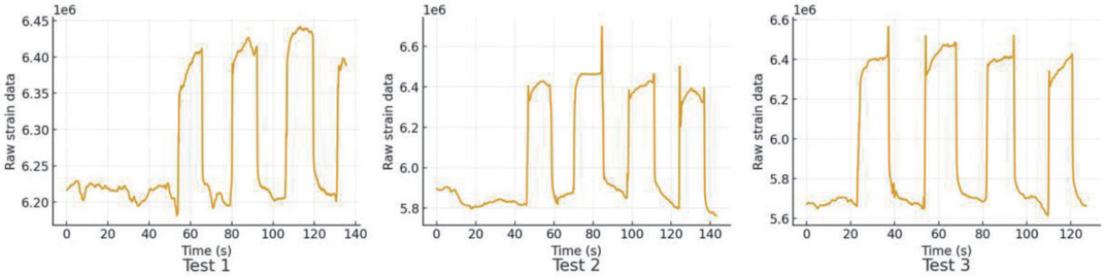

Fig. 18. (Color online) Sensor output data from repeatability assessment tests.

Table 2
Statistical evaluation results of repeatability.

	Mean force (N)	Std dev (N)	Std dev (%FS)	Max deviation
Test 1	0.0565	0.1116	1.12%FS	1.28%FS
Test 2	0.0565	0.0562	0.56%FS	0.63%FS
Test 3	0.0565	0.0852	0.85%FS	0.98%FS

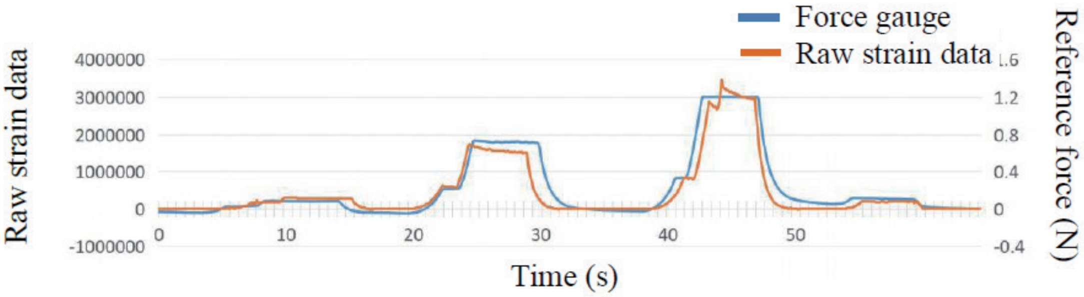

Fig. 19. (Color online) Dynamic response comparison of force sensor and reference force gauge.

For quantitative comparison, we computed the coefficient of determination R^2 and the Pearson correlation coefficient r between the two output signals. As summarized in Table 3, $R^2 = 0.992$ and $r = 0.996$. Values close to 1 indicate a very strong linear relationship and near-perfect positive correlation during dynamic measurement. We also quantified the response delay between the prototype sensor and the reference force gauge using MATLAB (MathWorks, USA). The time lag was estimated by computing the cross correlation between the two output signals and identifying the lag that yielded the maximum correlation. With a sampling period of 0.1 s, the resulting delay was approximately 0.2 s. This small delay indicates that the sensor output tracks changes in traction force with sufficiently low latency for real time visual feedback.

In summary, both the qualitative curve tracking and the statistical analysis show that the sensor enables the accurate and reliable tracking of time-varying tensile forces in real time, supporting precise force feedback during procedures.

Table 3
Statistical correlation analysis of the dynamic validation test.

R^2	*Corr* (r)	*Delay* (s)
0.992	0.996	≈ 0.2

5. Discussion

In this study, we proposed a traction microsystem with integrated real time force sensing for colorectal ESD. The work addresses the gap identified in the introduction, namely, the lack of controlled and quantitative traction in current practice. The system provides an integrated solution that combines active actuation with accurate force feedback. Common traction methods such as clip with line and S-O clip are mainly passive and provide uncontrolled or static tension.(3,6) They can be effective for simple lesions, yet limited control may result in inadequate visualization or tissue tearing. In contrast, the present system is operated with a joystick, allowing the operator to adjust traction force and wire extension in real time. This operator-driven control improves the ability to titrate exposure to the dissection plane.

A central innovation is the integrated force sensor. Although advanced methods such as the double scope technique allow dynamic traction, the applied force is typically judged subjectively by a second operator.(7) The sensor demonstrated high static linearity with $R^2 = 0.992$ and strong dynamic tracking with $R^2 = 0.992$ and $r = 0.996$, supporting the effectiveness of the custom 3D-printed sensing component. These results indicate the feasibility of low-cost, application-specific sensors for complex endoscopic procedures. In addition, the slip ring mitigates a practical limitation of wire-based traction by preventing twist accumulation during winding, which improves robustness and usability.

Several limitations should be acknowledged. First, the average repeatability of about 0.84% of full scale, while functional, is lower than typical specifications for commercial foil gauge sensors that are often below 0.2% of full scale, as discussed in Sect. 4.2. Within the clinical traction force range of 0.05 to 0.66 N, this corresponds to an absolute error of only a few millinewtons and is acceptable for visual feedback and safety monitoring. Contributing factors likely include properties of the 3D-printed substrate and small inconsistencies in manual fabrication and epoxy application, and long-term drift was not evaluated. Second, all validation was performed under *ex vivo* bench testing conditions. Performance in the *in vivo* colonic environment, where mucus, humidity, and peristalsis are present, has not yet been confirmed. We plan to evaluate the system first in colon models and later in animal colorectal ESD. In these studies, we will compare ESD with the present traction CA and the force sensor to ESD with conventional traction methods. The main outcome measures will include submucosal visibility scores, total procedure time, submucosal dissection time or dissection speed, en bloc and R0 resection rates, and the rates of perforation and post-ESD bleeding. We also plan to record the traction force data and the number of traction adjustments as quantitative indices of device use. By relating these indicators to the measured traction force, we intend to clarify whether real-time force feedback can improve visualization and efficiency without increasing adverse events, and to define practical target force ranges and safety thresholds for future clinical use. Third, although the traction CA is compact, the complete assembly, including the spiral scaffold, still requires space and careful delivery, which can be challenging in narrow or tortuous segments. In addition, the present prototype uses general purpose materials and has not been tested under repeated sterilization cycles, so its suitability for clinical sterilization has yet to be confirmed.

A further point is that the present sensor measures lead wire tension rather than the contact force at the lesion. In the bench tests, we reduced this difference by aligning the wire with the loading direction. During actual ESD, however, the effective force on the lesion can be reduced or redirected by friction at the traction ring and clip and by changes in wire path and traction angle. Therefore, the measured tension should be interpreted as a surrogate index of traction rather than as the exact lesion force. In future work, we plan to use colon models and systematically vary the traction direction to study the relationship between the sensor output and the actual lesion traction and to derive simple correction factors or safety thresholds that take wire angle and friction into account.

Future work will address these limitations. We will improve sensor design and fabrication to enhance repeatability, including the evaluation of alternative printing materials. Because the epoxy resin used to fix the lead wires may exhibit viscoelastic behavior due to its relatively large volume, we will investigate the effects of epoxy volume and explore alternative fixing materials to minimize such effects. For clinical use, the sensing structure and encapsulation will also need to be redesigned with more stable and sterilizable materials, and sensor performance after repeated sterilization cycles should be tested. Alternatively, a single-use approach could be explored, but its feasibility should be assessed together with cost and environmental considerations, including an economically feasible remanufacturing or recycling system. Building on these studies, we foresee three development aspects: further miniaturization of the motor, slip ring, and sensor to reduce the system size, improving clinical applicability, and the creation of closed loop traction control that uses real time force feedback to maintain target force levels with safety thresholds and automatic release strategies.

6. Conclusions

We reported a traction microsystem for colorectal ESD that integrates active traction, a slip ring for uninterrupted transmission, and a custom force sensor for real-time feedback. Designed for endoscopic delivery, the system enables controlled traction with continuous force monitoring.

Compared with clip with line and internal loop methods, the platform provides operator-controlled traction with quantitative feedback and endoscope compatibility, supporting improved precision and safety. The sensor showed high linearity with low mean absolute error and strong dynamic agreement with a commercial gauge, validating performance under both static and time varying loads.

Limitations include a lower repeatability than commercial gauge sensors and validation limited to *ex vivo* bench testing. Future work will improve repeatability and further miniaturize the modules to enhance clinical usability. In summary, the microsystem advances feedback-enabled, tool-assisted endoscopic microsurgery and lays the groundwork for future closed loop ESD support devices.

Acknowledgments

We are deeply grateful to Associate Professor Hisakata Maruyama of the Graduate School of Engineering, Nagoya University, for providing us with a colon model. This study was supported by JST (Moonshot R&D)(Grant Number JPMJMS2214–03).

References

1 S. Abe, S. Y. S. Wu, M. Ego, H. Takamaru, M. Sekiguchi, M. Yamada, and Y. Saito: Gut Liver **14** (2020) 673. https://doi.org/10.5009/gnl19266

2 H. Mizutani, S. Tanaka, and S. Oka: Clin. Endosc. **50** (2017) 562. https://doi.org/10.5946/ce.2017.108

3 K. Tsuji, N. Yoshida, H. Nakanishi, K. Takemura, S. Yamada, and H. Doyama: World J. Gastroenterol. **22** (2016) 5917. https://doi.org/10.3748/wjg.v22.i26.5917

4 H. Matsui, N. Tamai, T. Futakuchi, S. Kamba, A. Dobashi, and K. Sumiyama: BMC Gastroenterol. **22** (2022) 10. https://doi.org/10.1186/s12876-021-02085-w

5 M. Yoshida, K. Takizawa, S. Suzuki, Y. Koike, S. Nonaka, Y. Yamasaki, and H. Ono: Gastrointest. Endosc. **87** (2018) 1231. https://doi.org/10.1016/j.gie.2017.11.031

6 H. Ritsuno, N. Sakamoto, T. Osada, S. P. Goto, T. Murakami, H. Ueyama, H. Mori, K. Matsumoto, K. Beppu, T. Shibuya, A. Nagahara, T. Ogihara, and S. Watanabe: Surg. Endosc. **28** (2014) 3143. https://doi.org/10.1007/s00464-014-3572-0

7 T. Uraoka, S. Ishikawa, J. Kato, R. Higashi, H. Suzuki, E. Kaji, and K. Yamamoto: Dig. Endosc. **22** (2010) 186. https://doi.org/10.1111/j.1443-1661.2010.00992.x

8 T. Tanada, N. Tsuruoka, M. Fujishiro, Y. Tsuji, F. Arai, T. Yamaguchi, T. Nishi, and Y. Haga: Sens. Actuators, A **390** (2025) 116557. https://doi.org/10.1016/j.sna.2025.116557

9 N. Hagita, R. Kanai, H. Ishiguro, K. Minamizawa, F. Arai, F. Shimpo, T. Matsumura, and Y. Yamanishi: Sci. Robot. **9** (2024) eadg1842. https://doi.org/10.1126/scirobotics.adg1842

10 M. Nagata: World J. Gastroenterol. **28** (2022) 1. https://doi.org/10.3748/wjg.v28.i1.1

11 X. Gao, Y. Haga, N. Tsuruoka, W. Liu, Y. Sakaguchi, Y. Tsuji, M. Fujishiro, and F. Arai: Proc. 47th Annual Int. Conf. IEEE Engineering in Medicine and Biology Society (IEEE, 2025).